CHEMISTRY OF MATERIALS
Article

Chem. Mater. **2010,** *22,* 6529–6541 6529
DOI:10.1021/cm1017823

Urea-Melt Assisted Synthesis of Ni/NiO Nanoparticles Exhibiting Structural Disorder and Exchange Bias

Ana Querejeta-Fernández,[†] Marina Parras,[†] Aurea Varela,[†] Francisco del Monte,[‡] Mar García-Hernández,[‡] and José M. González-Calbet*,[†]

[†]*Departamento de Química Inorgánica I, Facultad de Ciencias Químicas, Universidad Complutense de Madrid, 28040 Madrid, Spain, and* [‡]*Instituto de Ciencia de Materiales de Madrid, CSIC, Campus de Cantoblanco, 28049 Madrid, Spain*

Received June 25, 2010. Revised Manuscript Received November 18, 2010

An easy, inexpensive urea-melt assisted route was designed for the synthesis of ~10 nm-sized Ni/NiO nanoparticles (NPs). The method consists of the thermal decomposition of a urea-melted medium containing a Ni^{2+}-salt and involves the olygomerization and self-combustion of the organic matrix and the formation of the Ni/NiO NPs within it in a two stepped process of Ni^{2+} reduction yielding Ni crystallization and subsequent inward oxidation. Control over the microstructural features of the NPs within three typical regimes was accomplished by means of the initial urea quantity. Type A samples (0.2 g urea/0.2908 g nickel nitrate) consists of NiO nanostructures which might contain dispersed Ni nuclei of a few atoms; B NPs (2 g urea/0.2908 g nickel nitrate) are made of proper small Ni cores, in the limit of the coherence length of XRD, surrounded by thick NiO shells, while C (20 g urea/0.2908 g nickel nitrate) NPs correspond to relative big Ni cores and thin NiO shells. Further control over the thickness of the NiO shell was achieved within each regime by means of the calcination time of the organic matrix, painting a whole palette of $Ni_{core}-NiO_{shell}$ NPs. Magnetic characterization revealed large (for A and B) and common (C) shifts of the hysteresis loops, which were ascribed to the high disorder of the (A, B and C) NPs obtained by quenching as well as to exchange bias (EB) effects (B and C). A thorough characterization of the reaction pathway is reported.

1. Introduction

The synthesis of ferromagnetic (FM) metals, such as Ni, Co, and Fe, at the nanoscale has been a subject of intense research because of their interesting magnetic properties.[1] Particularly, exchange bias (EB) phenomenology has attracted increasing attention as an effective means of overcoming the superparamagnetic limit typical of FM nanoparticles (NPs),[2,3] encountering thus promising applications in the fields of ultrahigh-density magnetic recording media,[4] spintronic devices[5] and medicine.[6] EB is manifested in systems where an antiferromagnetic (AFM) layer enhances the magnetic anisotropy of a nanosized FM component, preventing the ferromagnetic moments from fluctuating (superparamagnetism) because of thermal energy and such a sketch can be easily realized in metallic NPs surrounded by a metal oxide surface layer, that is, a core−shell structure. $Ni_{core}-NiO_{shell}$ NPs are especially promising in this field since, first, the Néel temperature of bulk NiO, 520 K, makes it suitable for generating EB at room temperature,[7] oppositely to CoO (T_N = 290 K[7]), and second, the relative difficult oxidation of metallic Ni NPs in comparison with Fe and Co NPs,[8] which spontaneously oxidize to a considerable extent upon exposure to air.[9,10] Furthermore, Ni/NiO NPs have been shown to find applications as anode materials for rechargeable batteries, ethanol fuel cells, and electrochemical capacitors,[11] as catalysts in organic reactions,[12] as hole-transport layer in LEDs[13] and have been used for magnetic separation of histidine-tagged proteins.[14]

*To whom correspondence should be addressed. E-mail: jgcalbet@quim.ucm.es.

(1) Kodama, R. H. *J. Magn. Magn. Mater.* **1999**, *200*, 359–372.
(2) Skumryev, V.; Stoyanov, S.; Zhang, Y.; Hadjipanayis, G.; Givord, D.; Nogués, J. *Nature* **2003**, *423*, 850–853.
(3) Iglesias, O.; Labarta, A.; Batlle, X. *J. Nanosci. Nanotechnol.* **2008**, *8*, 2761–2780.
(4) Martín, J. I.; Nogués, J.; Liu, K.; Vicent, J. L.; Schuller, I. K. *J. Magn. Magn. Mater.* **2003**, *256*, 449–501.
(5) Prinz, G. A. *Science* **1998**, *282*, 1660–1663.
(6) Häfeli, U., Schütt, W., Teller, J., Zborowski, M., Eds. *Scientific and Clinical Applications of Magnetic Materials*; Plenum: New York, 1997.
(7) Nogués, J.; Schuller, I. K. *J. Magn. Magn. Mater.* **1999**, *192*(2), 203–232.
(8) The reduction potentials of Ni^{2+} (E^0 = −0.257 V), Co^{2+} (E^0 = −0.28 V), and Fe^{2+} (E^0 = −0.447 V) indicate the following oxidation capability of the metallic elements: $Fe^0 > Co^0 > Ni^0$
(9) Peng, S.; Wang, C.; Xie, J.; Sun, S. *J. Am. Chem. Soc.* **2006**, *128*, 10676–10677.
(10) Tracy, J. B.; Weiss, D. N.; Dinega, D. P.; Bawendi, M. G. *Phys. Rev. B* **2005**, *72*, 1–8.
(11) Poizot, P.; Laruelle, S.; Grugeon, S.; Dupont, L.; Tarascon, J. M. *Nature* **2000**, *407*, 496–499.
(12) Park, J.; Kang, E.; Son, S. U.; Park, H. M.; Lee, M. K.; Kim, J.; Kim, K. W.; Noh, H. J.; Park, J. H.; Bae, C. J.; Park, J. G.; Hyeon, T. *Adv. Mater.* **2005**, *17*, 429–434.
(13) Caruge, J. M.; Halpert, J. E.; Bulović, V.; Bawendi, M. G. *Nano Lett.* **2006**, *6*, 2991–2994.

Published on Web 12/06/2010

The magnetic properties of Ni/NiO NPs are thoroughly determined by the textural and microstructural features of both components, as well as the interface (quantity, roughness, ...) between them. Such attributes are especially critical in nanosized crystals and are profoundly determined by the synthetic route employed. Thus, the design of processes for the preparation of Ni/NiO NPs, which allow for the control over those features, is of paramount interest.

Ni/NiO core−shell NPs have been previously obtained by both physical and chemical routes. Among the former, magnetron-plasma-based cluster beam deposition,[15] evaporation,[16] pulsed laser ablation,[17] arch-discharge,[18] and e-beam lithography[19] techniques offer highly crystalline and monodisperse particles with an outer thin (1−2 nm) oxide shell. On the other hand, chemical strategies offer a wider range of conditions to tailor the features of the resulting Ni/NiO NPs, and can be classified into two main blocks: (a) liquid phase routes and (b) calcination of organic matrices. The former is based either on (i) decomposition of a metal−organic precursor in an organic solvent[12,20−26] or (ii) chemical reduction of metal salts in aqueous or organic media.[27−29] While remarkable advances of such liquid phase routes are the preparation of colloidal monodisperse and size-controllable metallic nickel NPs and nanorods, stabilizers protecting the surface and used for such requirements generally hamper the formation of a robust, thick AFM NiO shell, although NiO NPs have also been reported.[12,23] Typical calcination methods,[30−33] besides making it difficult the control over size, size distribution, and aggregation,[30,33] are found to lead to either NiO NPs[33] or encapsulated-Ni NPs.[31] Between the two limit cases, that is, Ni and NiO NPs, a rich range of Ni/NiO composites, including $Ni_{core}-NiO_{shell}$ NPs, deserves additional attention because of both the close conversion between these two components at the nanoscale and to their promising magnetic phenomenology.

Despite the considerable amount of papers reporting on the synthesis of $Ni_{core}-NiO_{shell}$ NPs, both the control over NiO thickness, especially in the case of tiny Ni cores, and the clear establishment of the influence of the microstructural features on the magnetic phenomenology remain a challenge. In this sense, Li et al.[30] reported on the preparation of $Ni_{core}-NiO_{shell}$ NPs with three different thicknesses of the shell as a function of the calcination temperature of a glycerol matrix, although no structural or magnetic characterization were performed. Also, Roy et al.[27,34] reported the progressive transformation of Ni into NiO NPs by annealing at different temperatures the powders prepared by borohydride reduction method in aqueous solution and they proposed a metastable oxygen-stabilized tetragonal structure for Ni NPs. On the other hand, regarding the preparation of ligand-stabilized Ni−NiO colloids, Johnston-Peck et al.[25] obtained two shell thicknesses (2−3 nm maximum) in size-controlled NPs in the range of 8−24 nm, although the amorphous structure of the shells led to the absence of EB, while Winnischofer et al. stressed the important relevance of highly disordered atomic structures on the magnetic behavior of Ni/NiO NPs.[24,35] This issue was also addressed by Del Bianco et al.[36] in Ni/NiO systems produced by ball milling and hydrogen reduction, where a disordered NiO component embodied small Ni-enriched regions. Finally, in this sense, NiO NPs prepared by calcining a gel have been reported to exhibit large coercivities and loop shifts, which are similar effects to those associated with exchange coupled FM/AFM materials. However, because of the lack of detection of crystalline Ni phase, the authors related the anomalous magnetic behavior to a magnetic order different from that found in the bulk material, as assessed by numerical modeling.[32,37]

On the other hand, the use of urea either in aqueous or organic solvents has been widely reported for the synthesis of oxides, nitrides, and carbonates[38−41] However, its use as a viscous melted reaction media is more restricted, including the functionalization of carbon nanotubes at low temperature,[42] the thermal transformation of metal

(14) Lee, I. S.; Lee, N.; Park, J.; Kim, B. H.; Yi, Y. W.; Kim, T.; Kim, T. K.; Lee, I. H.; Paik, S. R.; Hyeon, T. *J. Am. Chem. Soc.* **2006**, *128*, 10658–10659.
(15) Zhou, Y. Z.; Chen, J. S.; Tay, B. K.; Hu, J. F.; Chow, G. M.; Liu, T.; Yang, P. *Appl. Phys. Lett.* **2007**, *90*, 043111.
(16) Löffler, J. F.; Meier, J. P.; Doudin, B.; Ansermet, J.-P.; Wagner, W. *Phys. Rev. B* **1998**, *57*, 2915.
(17) Sakiyama, K.; Koga, K.; Seto, T.; Hirasawa, M.; Orii, T. *J. Phys. Chem. B* **2004**, *108*, 523–529.
(18) Sun, X. C.; Dong, X. L. *Mater. Res. Bull.* **2002**, *37*, 991–1004.
(19) Fraune, M.; Rüdiger, U.; Güntherodt, G.; Cardoso, S.; Freitas, P. *Appl. Phys. Lett.* **2000**, *77*, 3815–3817.
(20) Cordente, N.; Respaud, M.; Senocq, F.; Casanove, M. J.; Amiens, C.; Chaudret, B. *Nano Lett.* **2001**, *1*, 565–568.
(21) Han, M.; Liu, Q.; He, J.; Song, Y.; Xu, Z.; Zhu, J. *Adv. Mater.* **2007**, *19*, 1096–1100.
(22) Leng, Y.; Li, Y.; Li, X.; Takahashi, S. *J. Phys. Chem. C* **2007**, *111*, 6630–6633.
(23) Jana, N. R.; Chen, Y.; Peng, X. *Chem. Mater.* **2004**, *16*, 3931–3935.
(24) Winnischofer, H.; Rocha, T. C. R.; Nunes, W. C.; Socolovsky, L. M.; Knobel, M.; Zanchet, D. *ACS Nano* **2008**, *2*, 1313–1319.
(25) Johnston-Peck, A. C.; Wang, J.; Tracy, J. B. *ACS Nano* **2009**, *3*, 1077–1084.
(26) Jeon, Y. T.; Moon, J. Y.; Lee, G. H.; Park, J.; Chang, Y. *J. Phys. Chem. B* **2006**, *110*, 1187–1191.
(27) Roy, A.; Srinivas, V.; Ram, S.; De Toro, J. A.; Mizutani, U. *Phys. Rev. B* **2005**, *71*, 184443.
(28) Grzelczak, M.; Pérez-Juste, J.; Rodríguez-González, B.; Spasova, M.; Barsukov, I.; Farle, M.; Liz-Marzán, L. M. *Chem. Mater.* **2008**, *20*, 5399–5405.
(29) Wu, S. H.; Chen, D. H. *Chem. Lett.* **2004**, *33*, 406–407.
(30) Li, Y.; Cai, M.; Rogers, J.; Xu, Y.; Shen, W. *Mater. Lett.* **2006**, *60*, 750–753.
(31) Koltypin, Y.; Gedanken, A. *Chem. Mater.* **1999**, *11*, 1331–1335.
(32) Makhlouf, S. A.; Parker, F. T.; Spada, F. E.; Berkowitz, A. E. *J. Appl. Phys.* **1997**, *81*, 5561–5563.
(33) Li, Q.; Wang, L. S.; Hu, B. Y.; Yang, C.; Zhou, L.; Zhang, L. *Mater. Lett.* **2007**, *61*, 1615–1618.
(34) Roy, A.; Srinivas, V.; Ram, S.; De Toro, J. A.; Riveiro, J. M. *J. Appl. Phys.* **2004**, *96*, 6782–6788.
(35) Nunes, W. C.; De Biasi, E.; Meneses, C. T.; Knobel, M.; Winnischofer, H.; Rocha, T. C. R.; Zanchet, D. *Appl. Phys. Lett.* **2008**, *92*, 183113.
(36) Del Bianco, L.; Boscherini, F.; Fiorini, A. L.; Tamisari, M.; Spizzo, F.; Antisari, M. V.; Piscopiello, E. *Phys. Rev. B* **2008**, *77*, 094408.
(37) Kodama, R. H.; Makhlouf, S. A.; Berkowitz, A. E. *Phys. Rev. Lett.* **1997**, *79*, 1393–1396.
(38) Sardar, K.; Dan, M.; Schwenzer, B.; Rao, C. N. R. *J. Mater. Chem.* **2005**, *15*, 2175–2177.
(39) Qiu, Y.; Gao, L. *J. Am. Ceram. Soc.* **2004**, *87*, 352–357.
(40) Qiu, Y.; Gao, L. *Chem. Lett.* **2003**, *32*, 774–775.
(41) Matijević, E. *Chem. Mater.* **1993**, *5*, 412–426.
(42) Ford, W. E.; Jung, A.; Hirsch, A.; Graupner, R.; Scholz, F.; Yasuda, A.; Wessels, J. M. *Adv. Mater.* **2006**, *18*, 1193–1197.

oxide NPs into nanocrystalline metal nitrides at high temperature,[43] and the synthesis of metal nitride particles[44] and NPs[45] and ternary metal oxynitride NPs.[46] It has also been used in a similar fashion as a source of nitrogen and carbon in concentrated ethanol solutions for the synthesis of metal nitrides and metal carbides NPs.[47]

Herein, we report a simple, inexpensive route for the synthesis of Ni/NiO NPs (~10 nm) with peculiar structural and magnetic properties. Interestingly, thick AFM shells and tiny FM cores are accessible. As far as we know, this is the first report of the synthesis of metal and metal oxide NPs by making use of urea as both reactant and reaction media. The magnetic behavior of the NPs has been evaluated and the coercivities and loop shifts of the three different types of prepared materials have been correlated with their proposed structures.

2. Experimental Section

Nickel nitrate hexahydrate ($Ni(NO_3)_2 \cdot 6H_2O$) (98.5%) and urea (99%) (Fluka) were used as received. First, Teflon vessels equipped with a Teflon cap were loaded with 1 mmol of $Ni(NO_3)_2 \cdot 6H_2O$ (0.2908 g) and four different amounts of urea (0.2 g sample A, 2 g samples B, 12 and 20 g sample C[48]). The vessels were closed with the cap and placed into an oven at 150 °C for either 2 or 16 h. It is noteworthy to note that urea does not melt if the vessels are left open. The homogeneous green liquids were cooled down at room temperature. Stirring of the products with a spatula before completely cooled is necessary to further handle them, especially in the high urea content experiments, which solidify as a hard block if not broken into smaller pieces before completely solids. Portions of the resulting green to blue oligomers were placed into porcelain crucibles, whose size was chosen to ensure a similar ratio (load's height/crucible's height), around a third, for series B and C samples. However, series A was always loaded as a thin layer because of the lower amount of matter in this case. Crucibles were put into a furnace and heated with a constant rate of 2 °C/min until 400 °C, kept at 400 °C during typical times of 2 h and cooled down within the furnace. Dark-gray powders were obtained. All the thermal treatments were performed within a fume hood.

Thermogravimetric and differential thermal analysis (TGA-DTA) of urea was measured under air on a Seiko Exstar 6300 instrument. Powder X-ray diffraction (XRD) of the as-prepared powders was carried out using a Siemens D5000 diffractometer with Cu Kα radiation (λ = 1.5418 Å). Quantitative analysis of the relative content of Ni and NiO phases was made by means of the reference intensity ratio (RIR) method[49] in the XRD patterns making use of the X'Pert High Score Plus v2.2d Panalytical BV software. Selected area electron diffraction (SAED) and transmission electron microscopy (TEM) was performed on a JEOL JEM-2000 FX electron microscope whereas high-resolution transmission electron microscopy (HRTEM) was carried out in a JEOL300FEG microscope. Scanning electron microscopy (SEM) was performed on a JSM-6330F FEG scanning electron microscope working at 20 kV. Surface composition of the NPs was studied by X-ray photoelectron spectroscopy (XPS) in a VG Escalab 200 R equipment. The textural properties of the samples were measured by N_2 sorption using a gas adsorption analyzer Micromeritics ASAP 2010 V.5 02. The presence of organic traces in the Ni/NiO powders was assessed by elemental analysis in a Perkin-Elmer, Series II 2400 Elemental Analyzer. Magnetization measurements at 2−325 K were obtained by SQUID magnetometry using a Quantum Design magnetometer equipped with a 5 T superconducting coil.

3. Results and Discussion

Compositional and Structural Characterization. Figure 1 collects XRD and TEM images of the three types (A, B, C) of NPs. XRD patterns can be assigned to rock salt NiO (JCPDS 00-47-1049) for A and B samples, whereas both rock salt NiO and fcc Ni (JCPDS 01−089−7128) phases are observed in C sample.[50] The relative mass ratio of both phases in sample C was determined from the XRD pattern making use of the RIR method: 74% of NiO and 26% of Ni. The low magnification TEM images illustrate the overview of the three samples. Sample A displays nanocrystals of around 10 nm (15.0 nm calculated from XRD by Scherrer method from the (111) peak) frequently highly interconnected into a continuous thin network. Voids between nanocrystals can also be observed as a result of incomplete sintering. In overall, sample A could resemble a porous matrix. It is worth noting that sporadic bigger (> 50 nm) crystals resulting from the sintering of the NPs from such a porous network are observed (see also the Supporting Information, Figure S1A). A slightly different morphology is shown for samples B and C, which display around 12 (16.1 nm by Scherrer) and 9 nm (15.0 nm by Scherrer), respectively, loosely aggregated NPs. As regards the connection among the NPs, it is worth mentioning that some flat sheets made up of NPs are found in B, although the network is not as continuous as in A, whereas even less continuous sheets of NPs are present in C (Supporting Information, Figure S1B and C, respectively). SAED patterns of the three samples (Supporting Information, Figure S2) reveal a random orientation among crystalline NPs (ring patterns) and show the presence of interplanar distances corresponding to rock salt NiO in A and B samples and both rock salt NiO and fcc Ni in C samples, in agreement with XRD data.

It is worth noting that different XRD-based Ni/NiO ratios were obtained for different batches (eight experiences per series, Table 1). For samples A, 100% NiO was always obtained, while samples B do show small Ni peaks in some cases and such a phase ranges from 0 to 7%. Samples C always show large Ni peaks.

(43) Buha, J.; Djerdj, I.; Antonietti, M.; Niederberger, M. *Chem. Mater.* **2007**, *19*, 3499–3505.
(44) Podsiadlo, S. *Thermochim. Acta* **1995**, *256*, 367–380.
(45) Gomathi, A.; Sundaresan, A.; Rao, C. N. R. *J. Solid State Chem.* **2007**, *180*, 291–295.
(46) Gomathi, A.; Reshma, S.; Rao, C. N. R. *J. Solid State Chem.* **2009**, *182*, 72–76.
(47) Giordano, C.; Erpen, C.; Yao, W.; Antonietti, M. *Nano Lett.* **2008**, *8*, 4659–4663.
(48) Since both 12 and 20 g urea samples display similar features, they are included in the C series.
(49) Chung, F. H. *J. Appl. Crystallogr.* **1975**, *8*, 17–19.
(50) It is worth mentioning that although the most frequent Ni structure is cubic, fcc; hexagonal, hcp; [2f,26] and highly disordered[24] Ni structures have been also found in NPs, while also amorphous[25] and NiO_2[28] structures have been proposed for the NiO shells apart from the typical cubic rock salt one.

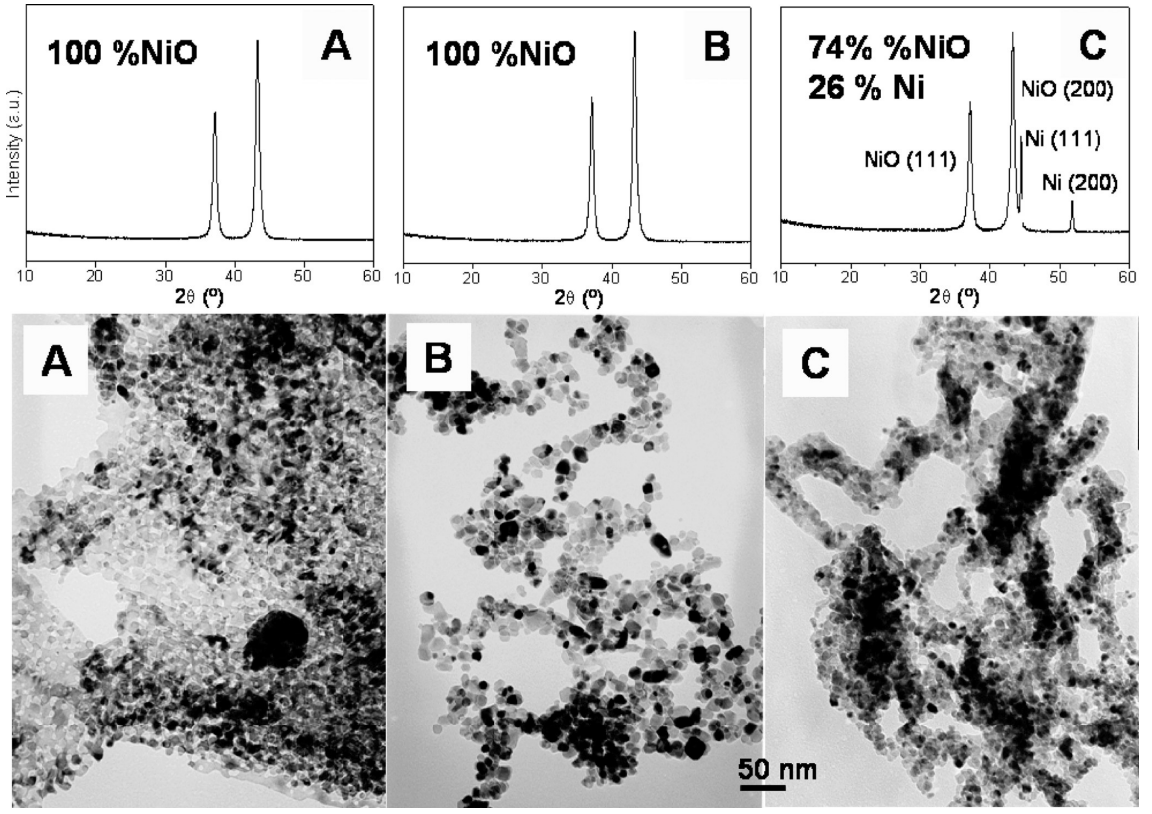

Figure 1. XRD patterns and TEM images of representative members of A (0.2 g urea), B (2 g urea), and C series (20 g urea) of as-prepared NPs. The samples were prepared by [150 °C, 16 h + 400 °C, 2 h] protocol.

Table 1. Average and Range NiO Percentage Calculated by RIR Method from the XRD Patterns for the Different Experiments Performed in Series A, B, and C NPs

	% NiO
A (0.2 g urea)	100 [100]
B (2 g urea)	98 [93−100]
C (12 g urea)	58 [48−74]
C (20 g urea)	54 [40−76]

The surface composition of A, B, and C NPs was evaluated by XPS, which reveals the presence of nickel oxide and nickel-hydroxyl bonds up to a maximum distance of 3 nm from the surface. In the Ni $2p_{3/2}$ region, a peak at a binding energy of 854.4 eV is ascribed to Ni^{2+} species (Supporting Information, Figure S3a).[51,52] Complementary O 1s spectrum shows two peaks at ~529.4 and 531.0 eV, which correspond to Ni−O−Ni and Ni−OH bonds, respectively (Supporting Information, Figure S3b).[52] Table 2 summarizes the ratios of both superficial components for the three samples. Since neither nickel hydroxide nor oxyhydroxide was detected by XRD or SAED, it is suggested that hydroxyl groups are randomly distributed as an amorphous outermost layer, in good agreement with earlier reports.[28] The lack of a peak at 852.6 eV in the Ni $2p_{3/2}$ region is a clear evidence of the absence of metallic nickel on the NPs' surface.[51] As the XRD data evidence the presence of metallic nickel in B and C samples, such a phase must exist in an inner core of the NPs at a depth not detectable by the penetration (up to 3 nm) of XPS. This demonstrates the existence of a NiO shell and the location of the Ni phase within the inner part of B and C NPs. Although the nature of such a metallic phase, either a continuous core (i.e., core−shell NPs) or discontinuous Ni/NiO core (i.e., nanocomposite) cannot be determined by this technique, the presence of crystalline Ni domains, whose size is smaller for B NPs as compared to C NPs, seems to indicate a core−shell nature for B and C NPs.

Complementary HRTEM characterization (Supporting Information, Figure S4) of the three types of samples confirms a NiO rock salt structure for all the NPs examined, which in the case of B and C samples further supports the existence of Ni as inner nuclei instead of separated Ni and NiO NPs. An apparent single crystalline nature of the particles is observed, as opposite to some polycrystalline NPs previously reported.[24,25,28] In the latter cases, the crystalline domains within a particle corresponded to the large metallic nickel cores. However, in our case, no metal fcc Ni cores could be directly observed in any case. In the case of C-26%-Ni sample, this is probably because of the relative smaller crystal size of the inner metal phase as compared to previous reports. However, HRTEM characterization of C-60%-Ni sample reveals a visible core−shell nature (Figure 2), illustrated by a shell of about 1.5−3.5 nm and an apparent amorphous core, which could be the result of the misalignment of both crystalline

(51) Grosvenor, A. P.; Biesinger, M. C.; Smart, R. S. C.; McIntyre, N. S. *Surf. Sci.* **2006**, *600*, 1771–1779.
(52) Biesinger, M. C.; Payne, B. P.; Lau, L. W. M.; Gerson, A.; Smart, R. S. C. *Surf. Interface Anal.* **2009**, *41*, 324–332.

Table 2. XPS Data Corresponding to A, B-100%-NiO, and C-40%-NiO Samples Prepared by [150 °C, 16 h + 400 °C, 2 h] Protocol[a]

Sample	Ni $2p_{3/2}$ BE (eV)	O 1s BE (eV) (Int.)	species (oxygen bonds)
A (0.2 g urea)	854.4	529.5 (63) + 531.0 (37)	85% Ni−O−Ni + 24% Ni−OH
B (2 g urea)	854.4	529.4 (69) + 531.0 (31)	83% Ni−O−Ni + 18% Ni−OH
C (20 g urea)	854.4	529.4 (64) + 530.9 (36)	83% Ni−O−Ni + 23% Ni−OH

[a] The calculated percentage of nickel oxide and nickel hydroxide species is included.

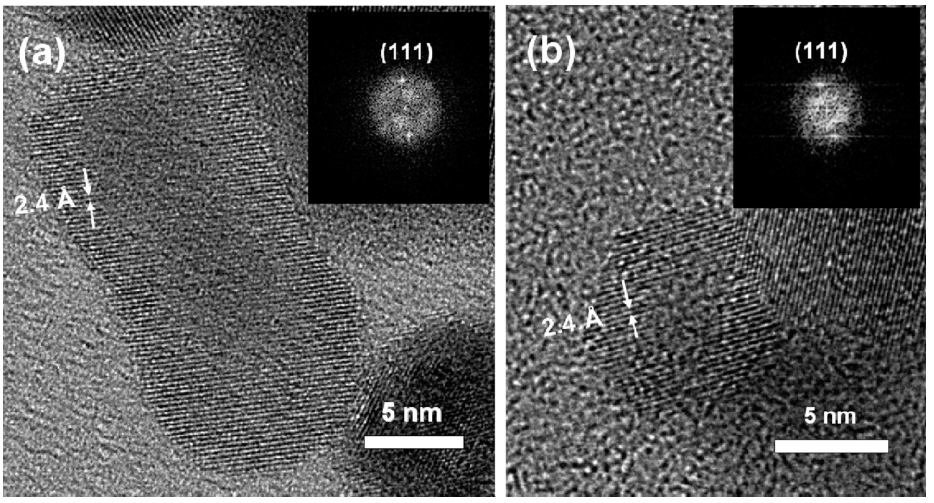

Figure 2. HRTEM images of $Ni_{core}-NiO_{shell}$ NPs corresponding to the C sample with 40% of NiO and 60% of Ni, prepared by [150 °C, 16 h + 400 °C, 2 h] protocol.

Ni_{core} and NiO_{shell} structures under the electron beam, in accordance with previous works reporting medium-thin NiO shells.[15] Nevertheless, such a core was not observed in the whole population of the particles, suggesting inhomogeneous volumes of the cores.

Further understanding of the different materials prepared can be achieved through a global inspection to the synthetic method. Crystallization of the metal nickel particles takes place at high temperature (400 °C) within a reducing organic decomposing matrix, (its self-combustion involves its oxidation, so it reduces the Ni^{2+} cations), which prevents NPs from hard aggregation and sintering and oxidation. After almost complete removal of the organics, the nickel NPs are exposed to the air, so diffusion of oxygen can take place from the surface inward. Such a dynamic oxidation process can be frozen by cooling down to room temperature, which might prevent the atoms from rearranging into a perfect NiO crystal and would likely lead to quenched Ni/NiO nanocomposites with a NiO shell characterized by high atomic disorder. In other words, unstable Ni NPs at 400 °C would suffer a spontaneous oxidation and subsequent unstable $Ni_{inner}-NiO_{shell}$ NPs at 400 °C could be quenched, leading to metastable (inert at room temperature) $NiO_{shell}-$Ni/NiO NPs; thus, the quenching process would freeze two metastable features: the defective crystallinity of a nanocrystal undergoing a dynamic process of oxygen diffusion and the thickness of the resulting NiO shell. In this sense, given that A, B and C samples were prepared under the same calcination conditions from different starting quantities of urea, the greater amount of organics in C requires of larger self-combustion times. Therefore, for equal calcinations times, series C metallic nickel NPs do not accomplish fully oxidation. This is the reason why the process in samples C does render larger Ni cores as compared to samples B. It is anticipated that samples A might also contain Ni nuclei, although the small crystal size, below the length coherence of XRD, would not be detectable by the diffraction experiment. Both the reaction mechanism and the magnetic characterization below are compatible with the presence of small metallic nickel nuclei in A samples. The metallic Ni phase (A < B < C) would be a consequence of the extension of the oxidative process from the surface inward suffered by the nickel NPs after removal of the organic matrix. In addition, it is reasonable to infer that Ni cores in samples C, besides their larger size as compared to A and B, present a broader particle size distribution, that is, small metallic Ni particles achieve almost complete oxidation for a certain calcination time, while this is not the case for intermediate and large size NPs. Besides, the thicker the passivating NiO_{shell}, the more hampered the advance of the oxidation would be, which would lead to Ni_{nuclei} size distributions in the sense A < B < C. On the other hand, since A samples are devoid of the organic matrix for longer times, as compared to B and C, a higher level of aggregation of the NPs is found, leading to some porous networks of aggregated NPs, which eventually form microcrystals because of sintering (Supporting Information, Figure S1; note also some sintering of the NPs along the same crystallographic direction in the corresponding HRTEM image in Supporting Information, Figure S4).

Therefore, control over external NiO thickness can be achieved depending on the amount of starting urea: the higher the urea content, the larger the Ni_{core} due to a shorter oxidative process. Similarly, it is easy to deduce that additional control over the thickness of the oxide shell can be accomplished by means of the calcination time, as detailed in the description of the reaction mechanism: longer calcinations times allow more penetrating oxidative processes.

Control over the relative Ni/NiO content is thus achieved for three regimes, A, B, C, which possess characteristic magnetic behavior stemming from typical levels of oxidation and microstructural features. Note, however, that the quenching nature of the synthesis makes it very sensitive to small differences in both heating and cooling rates, which could lead to the observed differences in the Ni/NiO ratio among different batches within a series (Table 1). In this sense, the larger differences among batches for C as compared to A and B samples reflect that C NPs are more sensitive to heating/cooling rates because the oxidation is easier at the outlayers of the NPs. It is worth mentioning that the same crucibles and quantities of Ni^{2+}-containing oligomer were used in all the experiments of a series, minimizing thus surface effects during combustion. Indeed, 100% NiO was obtained when very thin layers of oligomer were calcined, even for the highest urea content, pointing out toward a sacrificial oligomer outer layer in the crucible in good contact with an oxidizing air atmosphere which leads only to NiO NPs.

Magnetic Characterization. Further insights regarding the nature of the NPs were accomplished by magnetic measurements. All the samples were measured using a Quantum Designed SQUID magnetometer equipped with a 50 KOe coil. To avoid uncontrolled reduction of the samples at high temperatures in the He atmosphere of the instrument, magnetization versus temperature runs were limited to the temperature range 2−325 K using ZFC-FC protocols with $H = 50$ KOe as cooling field and $H = 50$ Oe as the measuring field. Data corresponding to representative samples of series A−B−C are given in Figure 3. As expected, the blocking temperature given by the maxima of the ZFC measurements increases as the Ni content and the size of the Ni-nucleus or Ni-core increases. Also, the size distributions, related to the widths of the ZFC peaks, broaden from A to C, in good agreement with the structural features previously described. Note that ZFC−FC runs for all series exhibit large irreversibilities even at the highest temperature explored, which suggests that magnetic frustration and disorder not only are present but dominates the magnetic properties, this being particularly true for systems type A and B.

Hysteresis cycles at 2 K were systematically measured after zero field, 10, and 30 KOe cooling runs along the temperature interval 300−2 K. Figure 4 plots the magnetic field dependence of magnetization as measured in ZFC, 10 and 30 KOe FC runs, for three representative members of series A, B, and C. Three different magnetic behavior are exhibited by samples of the series A, B and C. Samples of series A are dominated by the magnetic

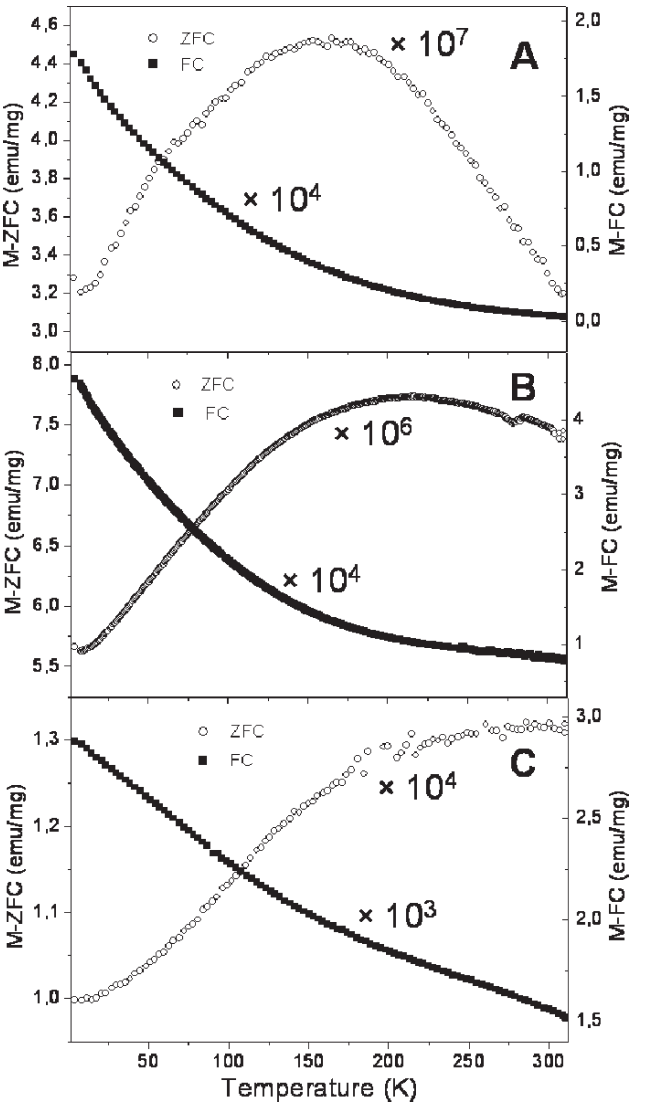

Figure 3. Plots of ZFC−FC runs of the magnetization versus temperature, as measured under 50 KOe cooling and 50 Oe measuring fields, for 100% NiO (A), 97% NiO (B), and 74% NiO (C) Ni/NiO NPs prepared by [150 °C, 16 h + 400 °C, 2 h] protocol.

response of a quite disordered AFM predominant component with small FM contributions evidenced by a small narrowing of the cycles around $H = 0$. Two possible hypotheses can be considered to explain the anomalous FM contributions in the AFM NiO matrix. On one hand, given the fact that no evidence for Ni nuclei is provided by other techniques, the neat magnetic moment observed could be ascribed to the existence of quite a number of unbalanced spins located at the surface and antiphase boundaries in the NiO AFM matrix, as it has been reported for NiO NPs.[32,37,53] However, since oxidation occurs from the outlayer toward the center of the particle and there is evidence for metallic Ni cores inside particles B and C, an alternative plausible interpretation is the existence of very tiny Ni nuclei inside the NiO matrix that would render short ranged FM correlations, as previously

(53) Feygenson, M.; Kou, A.; Kreno, L. E.; Tiano, A. L.; Patete, J. M.; Zhang, F.; Kim, M. S.; Solovyov, V.; Wong, S. S.; Aronson, M. C. *Phys. Rev. B* **2010**, *81*, 014420.

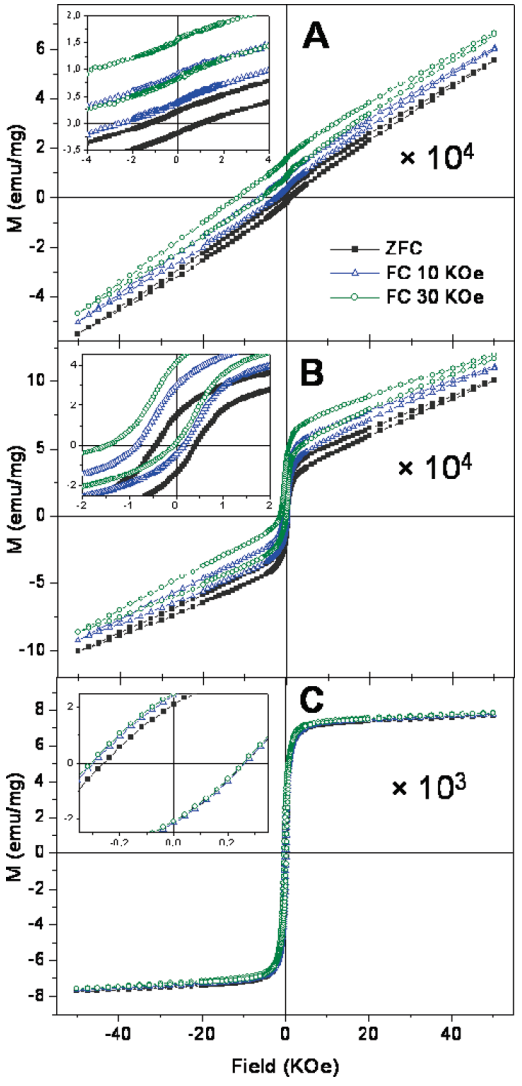

Figure 4. Hysteresis cycles measured at $T = 2$ K, recorded after a zero field, 10 and 30 KOe cooling protocols along the temperature interval 300−2 K for 100% NiO (A), 97% NiO (B) and 74% NiO (C) Ni/NiO NPs prepared by [150 °C, 16 h + 400 °C, 2 h] protocol. Insets show greater detail of the same measurements.

evaluated for Co/CoO NPs[10] and bilayers.[3,54] Both hypotheses would translate into large levels of magnetic disorder of the AFM matrix and would account for the irreversibility observed at the highest fields explored. Thus, within the magnetic description, we will refer to samples A as a disordered AFM NiO matrix, regardless of the proposed origins of the FM contribution, surface unbalanced spins plus antiphase boundaries or tiny Ni nuclei. Samples B show two neat contributions, one corresponding to FM Ni cores, whose size is just above the limit of the spatial coherence required to be detected by X-ray diffraction, and that of a thick NiO shell with large levels of magnetic disorder that translate into large irreversibility of the AFM component. Samples C cycles compel to what it is expected for well conformed FM Ni cores with the extra ingredient of a thin layer of AFM NiO, responsible for the slope observed at high fields. Figure 5 depicts the proposed models for A, B and C samples.

The analysis of the FM component has been done for samples with well-defined FM contribution, that is for series B and C. Although values for H_c, M_s, M_{ex}, and H_{ex} (defined below) have been extracted for series A, as an orthodox FM contribution is absent, these values refer to the disordered AFM contribution. Consequently, they cannot be compared to the values measured for series B and C, for which a well conformed FM core exists. The saturation values of the magnetization have been determined by extrapolation to $H = 0$ Oe of the slope assigned to the AFM contribution, with M_{sat} being the value corresponding to the intersection of such a slope with the M axis. As can be seen in Figure 6, M_{sat} and the remanent magnetization increase almost linearly with Ni content. The observed small deviation from linearity can be probably ascribed to the existence of disorder at interfaces. Also, the coercive field H_c decreases with Ni content (Figure 7 a) and, therefore, with increasing the FM particle size, compatible with the existence of various FM domains

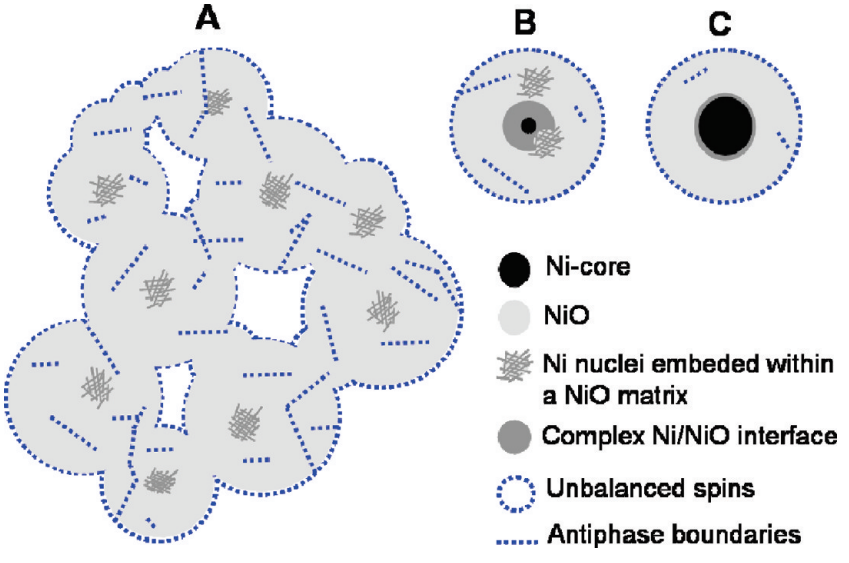

Figure 5. Proposed models of A, B, and C samples, contemplating all the possible contributions to the magnetic phenomenology.

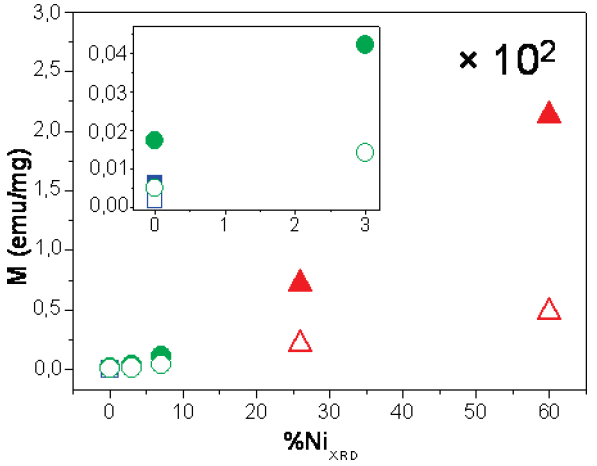

Figure 6. Magnetizations of saturation (solid symbols) and remanence (open symbols) vs "crystallographic" percentage of Ni phase for A (blue squares), B (green circles), and C (red triangles) members of Ni/NiO NPs prepared by [150 °C, 16 h + 400 °C, 2 h] protocol. Inset shows greater detail of the left zone of the same graph.

within the Ni cores[55,56] or a larger density of defects for series B than C. However, the smallness of the Ni cores makes the existence of multidomain clusters unlikely and the observed behavior is probably more related to the different defect density as the oxidation progresses during the synthesis. Also, it should again be kept in mind that the very high values shown by samples A cannot be compared to those of series B and C since they do not refer to well-defined FM entities.

Exchange bias (EB) is present in systems where a ferromagnet shares an interface with a larger magnetic anisotropy antiferromagnet, so the latter can pin the orientation of the FM component bellow the Néel temperature. Given the large number of interfaces intimately connecting FM Ni and AFM NiO in our samples EB effects are expected. Figure 4 shows large offsets for the ZFC and FC hysteresis loops of samples type A and B, while samples C are less affected by the cooling field. The effect is strongly enhanced for samples A and B where a large vertical shift (along M axis) is observed, pointing out toward the existence of a spin-glass like system corresponding to a highly disordered AFM NiO NP containing a large number of antiphase boundaries and surface unbalanced spins or, alternatively, some FM Ni nuclei. This is quite opposite to what it is observed in series C for which a more conventional, although small, horizontal shift (along axis H) exists, indicating that disorder in this series is comparatively less important.

To quantitatively assess the magnitude of the observed shifts, we have redefined a new coordinate system with origin at the center of each measured FC cycle. Hysteresis cycles keep the expected symmetry properties in the new coordinate system. Vertical and horizontal shifts

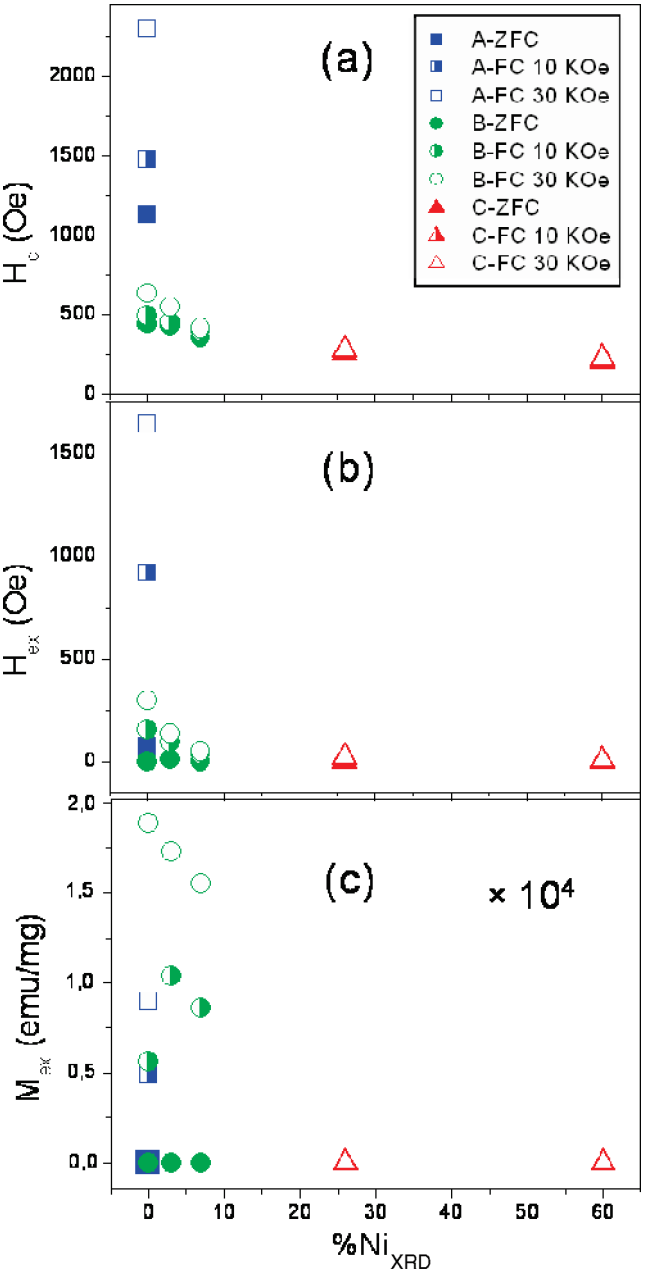

Figure 7. Ni_{XRD} mass percentage dependence of (a) coercive field (H_c), (b) H_{ex}, and (c) M_{ex}, for zero field, 10, and 30 KOe protocols at 2 K.

Table 3. H_c, H_{ex}, and M_{ex} Values for 30 KOe Protocols Corresponding to the Samples within Each Series A, B, and C

	H_c (Oe)	H_{ex} (Oe)	M_{ex} (emu/mg)
A (sample 100% NiO)	2298	1646	9.0×10^{-5}
B (sample 100% NiO)	635	298	1.89×10^{-4}
C (sample 74% NiO)	281	24	0

(M_{ex} and H_{ex}, respectively) are then given by the displacements of the new axis relative to the old coordinate system. M_{sat} and H_c are then directly read in the new coordinate system. Table 3 collects the calculated values of H_c, H_{ex}, and M_{ex} for the samples within each series A, B, and C.

As shown in Figure 7 b, the horizontal shift, given by H_{ex}, decreases as the Ni core size increases. The small bias

(54) Papusoi, C.; Hauch, J.; Fecioru-Morariu, M.; Guntherodt, G. *J. Appl. Phys.* **2006**, *99*, 123902.
(55) Cullity, B. D.; Graham, C. D. *Introduction to Magnetic Materials*; 1st ed.; John Wiley & Sons, Inc.: Hoboken, New Jersey, 1972; p 387.
(56) Leslie-Pelecky, D. L.; Rieke, R. D. *Chem. Mater.* **1996**, *8*, 1770–1783.

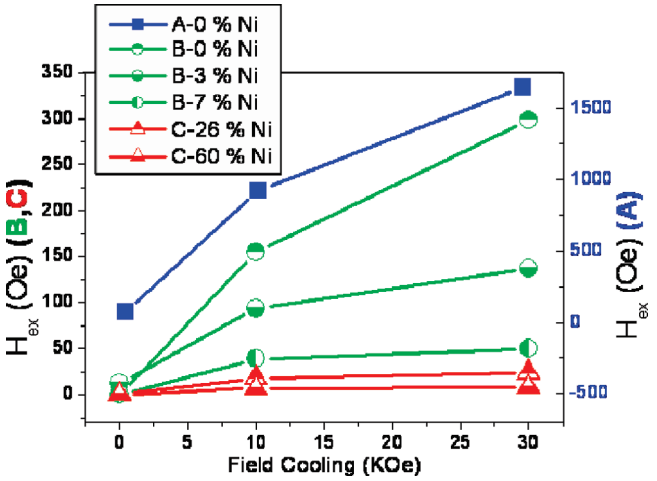

Figure 8. H_{ex} dependence of the cooling field for different members of A, B, and C series of samples.

field in samples C can be understood in terms of a less robust AFM of the thinner NiO shell when compared to that of series B.[57] H_{ex} for series A diverges, consistently with the already mentioned lack of a proper FM core and its glassy features. Hence, the hysteresis offset in series A cannot be explained in terms of an exchange anisotropy, but it is rather the result of the strong disorder and magnetic frustration in the systems. Here, metallic Ni, if at all present, is mainly as tiny clusters and crystal defects that contribute to the high disorder of the AFM NiO matrix and promote the observed spin glass-like behavior. Another precursor of the glassy contribution is the markedly different morphology of samples A, packed with nanovoids that seem to be absent in samples of series B and C.

The vertical displacement of the field cooled cycles, given by M_{ex}, is large for samples of series B (Figure 7c) and does not occur for samples C. This is compatible with the existence of interfaces affected by some level of disorder between proper FM cores (only present in samples B and C) and the AFM matrix, being this interfacial contribution much more obvious for sample B since the number of interfaces is larger that in series C. Also a better conformation of the FM cores in series C contributes to better structured interfaces that are less affected by disorder.

As expected, for a particular sample, H_{ex} increases with the applied cooling field (Figure 8). The values for series A are much larger and separated from the trend observed in series B and C, the reason being that the component rendering these values in series A is not an orthodox FM contribution but it rather corresponds to the analysis of a disordered AFM matrix. Consequently, loop shift cannot be explained in terms of EB effects for A NPs. Notice that the cooling field dependence of H_{ex} for series B and C does not follow a linear behavior, which again puts forward the important role of interfaces. Also, the observed increase of the FC coercivity as the cooling field is increased can be understood in such frustrated and disordered systems in terms of the coercive force necessary to bring the thermoremanent magnetization to zero and, therefore, it increases with the cooling field.

To determine the magnetic behavior at room temperature, the hysteresis cycle at 300 K for the B-0% Ni sample was measured (Supporting Information, Figure S5). H_{ex} and M_{ex} are 0, as expected, and H_c is of the same order of magnitude than the ZFC cycle at 2 K.

Overall, on the basis of the compositional characterization and magnetic behavior discussed, we suggest the following crystalline and structural features for the three samples (see Figure 5). Series A consists of a nanostructured NiO matrix that might contain inner Ni nuclei of a reduced number of atoms. The most relevant feature is the high disorder, leading to the large irreversibilities observed. The presence of tiny Ni nuclei could be compatible with the FM contributions to the magnetic properties, although unbalanced spins in the AFM matrix would render the same phenomenology including (i) the small narrowing of the cycles around $H = 0$ and (ii) large vertical shifts in the magnetic hysteresis effects. Further insights regarding the presence of tiny Ni nuclei are discussed below on the basis of performing the reaction with four different quantities of urea and three calcination times for each urea quantity, which allows one to deduce the time-line vision of the oxidative process. The absence of an orthodox Ni core in A samples is supported by (a) the absence of the corresponding peaks in XRD patterns and (b) the absence of a proper FM hysteresis cycle. Regarding to series B, NPs are made up of a proper metallic nickel core, whose size is around the limit of the length coherence for XRD, surrounded by a thick and atomically disordered AFM shell. An O-deficient NiO intermediate zone between the core and shell is plausible to be present. The Ni/NiO interface and, in turn, the disorder, is lower than for A and larger than for C samples. EB effects are encountered in B and C samples. Samples C correspond to well conformed FM Ni cores, with a broader size distribution than the corresponding to B samples, in an ordered frontier with a thin layer of AFM NiO, which leads to conventional EB effects and smaller shifts in the measured loops.

Mechanism of Reaction. Further comprehension of the route is reported in this section. We followed the course of the reaction by a combination of TGA-DTA measurements of urea (Supporting Information, Figure S6) and XRD analysis at different stages of the synthetic process (Supporting Information, Figures S7 and S8). Note that both Supporting Information Figures S7 and S8 collect the whole net of experiments build from four different starting quantities of urea, horizontal direction, and different temperatures and times of calcination, vertical direction, being the difference between both figures the first step of heating at 150 °C in the oven: 2 h for the former and 16 h for the latter. Supporting Information Figure S6 shows that after urea melts (melting point 133 °C[42]), its decomposition and oligomerization take place from

(57) Nogués, J.; Sort, J.; Langlais, V.; Skumryev, V.; Suriñach, S.; Muñoz, J. S.; Baró, M. D. *Phys. Rep.* **2005**, *422*, 65–117.

~140 °C up to ~170 °C in an endothermic process according to eqs 1−3:[44]

$$NH_2CONH_2 \rightarrow NH_4^+NCO^- \rightarrow NH_3 + HNCO \text{ (isocyanic acid)} \quad (1)$$

$$NH_2CONH_2 \rightarrow H_2O + H_2CN_2 \text{ (cyanamide)} \quad (2)$$

$$NH_2CONH_2 + HNCO \rightarrow H_2NCONHCON_2H \text{ (biuret)} \quad (3)$$

Additional decomposition of urea takes place in the presence of water (note the hydration water of the nickel salt) according to the eqs 4 and 5.

$$NH_3 + H_2O \rightarrow NH_4^+OH^-; NH_4^+OH^- + H_2NCONH_2 \rightarrow 3NH_3 + CO_2 \quad (4)$$

$$HNCO + H_2O \rightarrow CO_2 + NH_3 \quad (5)$$

Thus, during the first step of thermal treatment at 150 °C in the oven, the homogeneous Ni^{2+}-solution (as evidenced by the green color of the liquid) contains mostly melted urea (JCPDS 01-072-0118) at 2 h (Supporting Information, Figure S7, first row) and urea and biuret (JCPDS 00-011-0732) if further decomposition and oligomerization are allowed at longer times, 16 h (Supporting Information, Figure S8, first row). Such compounds are predominant at higher urea/Ni ratios, while for low ratios urea is not allowed to oligomerize as pure biuret, so a different crystalline pattern is obtained at 2 h. Such intermediate evolves to ammonium nitrate (JCPDS 01-070-1443) at 16 h of thermal treatment. Pictures of the oligomers obtained at 2 and 16 h of thermal treatment are collected in Figure 9.

According to TGA-DTA, further thermal treatment from 170 to ~240 °C allows a second and third end othermic processes to take place (Supporting Information, Figure S6), which matches well with the reported formation of triurea (eq 6) and dicyandiamide around 210 °C (eq 7).[44]

$$H_2NCONHCON_2H + HNCO \rightarrow H_2NCONHCONHCONH_2 \text{ (triuret)} \quad (6)$$

$$2H_2CN_2 \rightarrow H_4C_2N_4 \text{ (dicyandiamide)} \quad (7)$$

Next, between ~240 and ~300 °C a stable compound is obtained (as evidenced by a small plateau in TGA-DTA, Supporting Information, Figure S6). Such a stable compound is detected upon a second stage of calcination of the Ni^{2+}-oligomer in a furnace at 300 °C and is indexed as cyanuric acid (JCPDS 00-023-1637) (Supporting Information, Figure S7, second row, and Figure S8, second row), which is an aromatically stabilized, cyclic trimer ($(HNCO)_3$) of isocyanic acid. Note that two extra reflections of low-medium intensity appear at 10.7 and 27.9° (2θ), which are attributed to ammelide ($C_3H_4N_4O_2$) (JCPDS 00-031-1527), also produced in the decomposition of biuret but a slower rate than cyanuric acid. Actually, if higher calcination temperatures, that is, 360 °C (Supporting Information, Figure S7, third row), are used, only reflections of ammelide are observed in the XRD pattern. Although other compounds such as ammeline, melamine and melame have been reported to form in small quantities upon decomposition of urea,[44] no corresponding peaks have been observed in our case.

If the Ni^{2+}-oligomer obtained in the first step of our route is treated at 400 °C, above the decomposition temperature of aromatically stabilized cyanuric acid ($T_{\text{maximun rate of decomposition}}$ = 400 °C) and ammelide (T_{mrd} = 420 °C),[44] complete self-combustion of the crystalline organic matrix takes place releasing H_2[44] and leading to the reduction of Ni^{2+} cations to Ni. Loosely aggregated metal nickel NPs are thus allowed to crystallize at high temperature protected by the matrix, which is amorphous after 1 h of thermal treatment for the sample with the highest urea content (Supporting Information, Figure S7, fourth row, fourth column) and is completely removed after 2 h at 400 °C (Supporting Information, Figure S7, fifth row, fourth column), resulting in an outer oxidation of the Ni NPs. The NiO shell protecting the metal cores spreads via oxygen diffusion from the outside toward the center of the particles at longer combustion times, as evidenced by the facts that (i) global size of the particles remains approximately unchanged (results not shown) and (ii) NiO/Ni ratio increases as the time of calcination at 400 °C increases up to 4 h (Supporting Information, Figure S7, sixth row, fourth column). In addition, the NiO core can be manipulated in another way: the lower the urea content, the faster the self-combustion takes place, the higher NiO/Ni ratio. Thus, NiO NPs are formed even at 300 °C for the lowest urea content (Supporting Information, Figure S7, second row, first column). All in all, a whole palette of grades of oxidation, that is, $Ni_{nuclei}-NiO_{shell}$ NPs, is accessible by means of the manipulation of the urea content and calcination time, as shown in Supporting Information, Figure S7. Figure 9 summarizes the synthetic route.

Last, we will discuss the influence of the homogenization time of the Ni salt into the urea melted media at 150 °C (compare Supporting Information, Figures S7 and S8, first rows. Also, pictures of the resulting oligomers are shown in Figure 9). Obviously, longer times allow the formation of more biuret and triuret from urea, biuret and cyanic acid (eq 3 and 6), and the resulting consumption of cyanic acid translates into its minor availability to form aromatically stabilized cyanuric acid and ammelide, which are formed less efficiently and can be removed more efficiently at 400 °C. As a result, remaining organic elements in the powders are significantly lower for longer treatments of the melted media at 150 °C, as evidenced by elemental analysis measurements (Supporting Information, Table S1). Therefore, we chose the samples treated at 150 °C during 16 h for the magnetic characterization, given the absence of diamagnetic contribution. Last, elemental analysis results (Supporting Information, Table S1)

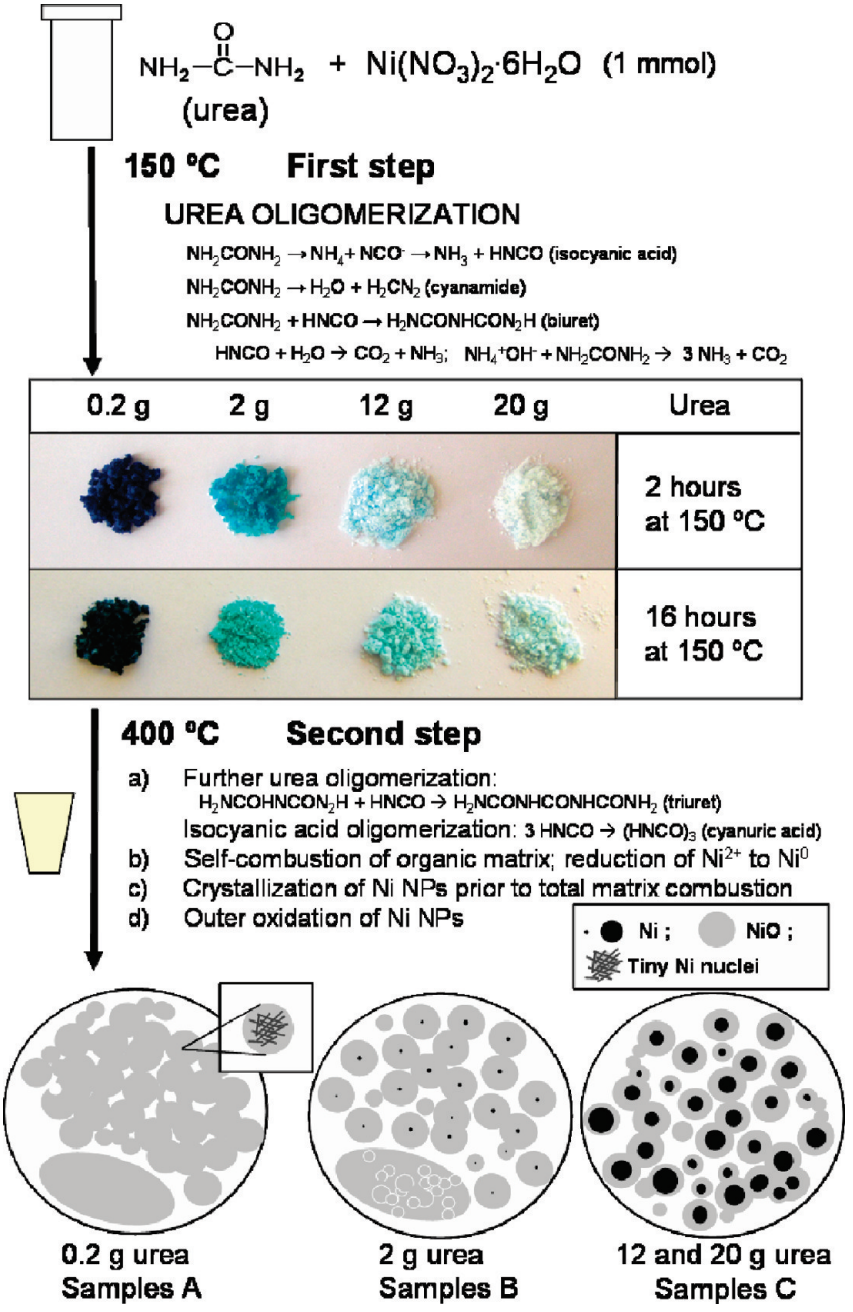

Figure 9. Summary of the synthesis procedure and formation mechanism of A, B, and C Ni/NiO nanostructures. Pictures of the blue to green oligomers obtained after thermal treatment at 150 °C for two different times (2 and 16 h) are shown. On the bottom, the proposed microstructural models for the nanostructures.

verified that, for equal previous thermal treatments at 150 °C, longer calcination times lead to lower amount of organic traces due to a more efficient combustion.

Control over the Ni/NiO Ratio, Oxidation Process, and Nonstoichiometry. It is important to emphasize that the NiO/Ni mass ratios calculated in this paper refer to the crystallographic components able to be detected by the XRD experiment. In this sense, there is evidence that B-0%-Ni NPs, whose XRD pattern does not show a Ni peak, contain a small Ni_{core} since they exhibit the same magnetic regime than B-3%-Ni NPs batch displaying proper FM contributions (Supporting Information, Figure S9b and c shows the XRD patterns of B-3%-Ni and B-7%-Ni NPs, respectively). Hence, XRD may not be a valid way to detect tiny crystals, which would be ignored by the technique. In our case, both A and some B samples present XRD-based-100%-NiO and consequently an alternative assessment of the presence of tiny $Ni_{nuclei/cores}$ is desired. While magnetic characterization of B samples is quite compelling regarding the presence of Ni_{cores}, magnetic effects displayed by A samples cannot unambiguously be attributed to tiny Ni nuclei, and thus, further insights are desired.

Attempts to better understand the formation of the NPs were done by XRD-evaluation of the products obtained for four different urea quantities and three calcination times for each urea quantity (Supporting Information, Figure S7). Here, XRD is a useful technique for relative

rather than absolute values; i.e. for comparing products and extracting trends. First, for equal calcination times, as it has already been noted, the NiO/Ni ratio is higher for lower urea amounts (e.g., for 2 h of calcination, 100, 98, and 67% NiO is obtained for 0.2, 2, and 20 g urea, respectively) because of the faster self-combustion of the matrix and, thus, longer oxidation processes of the metallic NPs. Second, let us fix now the urea amount. In the 20 g urea experiments (forth column), the organic matrix is not removed at 1 h of calcination and no Ni/NiO is detected (fourth row), while for 2 h the content of NiO is 33% and for 4 h is 57% NiO (fifth and sixth rows). Such an increase of NiO phase at the cost of the decrease of Ni phase at longer times must be caused by the oxidation of the metal phase and given that the NPs at 2 h have a core−shell nature, as extracted from the combination of XRD, large Ni peaks, and XPS, with no Ni at the surface, the oxidative process should take place from the surface inward. If one performs the same experiment with lower urea content, the same mechanism should be expected. Thus, for 2 g urea (second column), 85% NiO is obtained at 1 h of calcination (fourth row) and longer calcination times lead to the increase of oxide at the cost of the decrease of the metallic phase: 98% NiO and 100% NiO are obtained at 2 (fifth row) and 4 h (sixth row), respectively. (Supporting Information, Figure S9a shows greater magnification of the 98% NiO XRD pattern extracted from Figure S7, the purpose being to remark the incipient, almost not detectable Ni peaks). Keeping this trend in mind, it seems feasible that a situation can be achieved in which the outer oxidation of the metallic Ni NPs is so deep that the remaining Ni nuclei are too small to be detected by XRD. Certainly, that situation should be achievable in a continuous oxidation of a metal phase; reaching it is just a matter of finding the accurate experimental conditions, represented by urea content and calcination time, to stop the oxidation process at the accurate point. Actually, that must be the case of B-0%-Ni NPs; slight differences in the heating/cooling rates among batches lead to 0, 3 or 7% Ni for B samples. In the case of A samples, we speculate with the possibility that tiny Ni nuclei remained free of oxidation. Such Ni nuclei or crystal defects would account, at least to some extent, for the unorthodox FM component manifested in the magnetic phenomenology. Experimentally, no detection of Ni phase could be done for 0.2 g urea (first column) at any calcination time (1, 2, 4 h; forth, fifth, sixth rows) and even at lower calcination temperatures (300, 360 °C; second, third rows). Consequently, the "Ni defects" of samples A are a speculation and, analogously, the intermediate zone between the Ni_{core} and NiO_{shell} in B samples is speculated to be a disordered, O-deficient NiO. More interestingly, it is claimed that XRD, which "detects" order, may not be a suitable technique for assessing the purity of NiO NCs, above all if prepared by organic matrix calcination routes characterized by both reduction and oxidation steps, since "disorder" stemming from unoxidized Ni atoms could remain. Therefore, previous interpretations relative to the magnetic anomalies of NiO NPs[32,37,53] might need to be revised and the hypothesis of Ni tiny nuclei might need to be taken into account in this field.

The hypothesis proposed herein relative to nonstoichiometry is in consonance with previous studies in the Co/CoO system, for which an intentional oxidation of native colloidal Co NPs allowed the detection of three different oxidation extents exhibiting magnetic anomalies, which were attributed to clusters of a few unoxidized Co atoms within a CoO phase.[10] Other experimental and simulation results in bilayers further reinforce this sketch.[3,54] Furthermore, this situation should be more prone to occur in the Ni/NiO than in the Co/CoO system given the more difficult oxidation of the former metal.[8]

Finally, it is worth remarking the differences between our process and other deliberated oxidations of Ni NPs at elevated temperatures.[58,59] In the latter reports, hollow NiO NPs are produced as a result of the nanoscale Kirkendall effect resulting from a much faster outward diffusion of nickel than the inward diffusion of oxygen. The enhanced mobility of nickel ions in such cases may be favored by the grain boundaries in the polycrystalline native Ni NPs. This might be opposite to our monocrystalline primitive Ni NPs, which would likely account for a preferential oxygen diffusion leading to solid NiO NPs.

We hope that the observations reported herein stimulate further endeavors toward the rich Ni/NiO nanostructured system from experimental, characterization and theoretical perspectives. The ability to control the microstructural features of the Ni/NiO NPs should eventually open the path to materials benefiting from the enhanced thermal stability of a small FM component embedded within an air-stable NiO component susceptible of functionalization and, thus, of manufacturing for a wide range of potential applications.[4−6,11−14]

4. Conclusions

In summary, an easy, inexpensive urea-melt assisted synthetic route has been designed for the synthesis of Ni/NiO NPs. It is believed that the synthetic method reported here can be extended to other metallic or oxide NPs. Herein, microstructural features of the as-prepared NPs can be controlled for three typical regimes (A, B, C) as a function of the starting urea quantity: the lower the urea amount, the thicker the NiO_{shell}. Additionally, extra control over the fraction of NiO_{shell} within each regime was achieved by means of the calcination time: longer calcinations lead to deeper oxidations. On the other hand, organic matter in the resulting products was found to minimize at 16 h of previous thermal treatment at 150 °C of Ni^{2+} salt and urea, allowing for a magnetic characterization without diamagnetic contribution. While XPS demonstrates the presence of a NiO_{shell} in A, B, and C samples, the existence of Ni_{cores} in samples B and C is strongly supported by XRD, as well as the observed

(58) Nakamura, R.; Lee, J. G.; Mori, H.; Nakajima, H. *Philos. Mag.* **2008**, *88*, 257–264.
(59) Railsback, J. G.; Johnston-Peck, A. C.; Wang, J.; Tracy, J. B. *ACS Nano* **2010**, *4*, 1913–1920.

magnetic properties (and also HRTEM for C samples). The formation mechanism additionally points out toward the presence of Ni_{cores} in those B samples whose XRD patterns do not show a Ni peak. In the case of samples A, where no Ni at all is detected either by XRD and HRTEM, both the formation mechanism and the magnetic properties are compatible with tiny Ni nuclei, although there is no evidence of such entities. This work puts forward the important role of disorder and quality of the interfaces between FM and AFM components in the global magnetic phenomenology. The defective crystallinity of the NPs reported here is because of a 2-fold reason: (a) inclusions of a metallic phase within a metallic oxide phase, which leads to a large FM/AFM interface rich in defects, and (b) the quenching of the nanocrystals undergoing oxygen diffusion. The observed magnetic behavior, in particular the large loop shifts observed for B NPs, is remarkably different compared it with previous reports on Ni/NiO NPs,[21,22,24,25,36] whereas the large loop shifts exhibited by A nanostructures resemble those displayed by previous reports on NiO NPs and interpreted on the basis of surface or antiphase boundaries effects.[32,37,53]

Acknowledgment. Financial support from MICINN projects CSD2009-00013, MAT2007-61954, MAT2008-06517-C02-01, and MAT2009-10214 is greatly appreciated. A.Q.-F. acknowledges MEC for financial support through a FPU PhD fellowship. The authors thank Dr. J. García Fierro for collecting and discussing the XPS spectra, Dr. E. Matesanz and Dr. J. Velázquez (Centro de Difracción de Rayos X UCM) for technical assistance and for their help with the RIR method, and Dr. A. Gómez Herrero and Dr. E. Urones Garrote (Centro de Microscopía Electrónica Luis Bru UCM) for their help with the acquisition of the HRTEM and SEM images.

Supporting Information Available: TEM, HRTEM, and SEM images, SAED and XRD patterns, XPS spectra, hysteresis cycle, nitrogen physisorption isotherms results, elemental analysis results and TG-DTA curve of urea, and description of textural properties. This material is available free of charge via the Internet at http://pubs.acs.org.